Available online at www.sciencedirect.com
ScienceDirect
Journal of Membrane Science 299 (2007) 236–250
journal of MEMBRANE SCIENCE
www.elsevier.com/locate/memsci

# The influence of membrane formation parameters on the functional performance of organic solvent nanofiltration membranes

Yoong Hsiang See-Toh, Frederico Castelo Ferreira [1], Andrew G. Livingston *

*Department of Chemical Engineering and Chemical Technology, Imperial College London, Exhibition Road, London SW7 2AZ, UK*

Received 25 October 2006; received in revised form 24 April 2007; accepted 30 April 2007
Available online 3 May 2007

**Abstract**

This paper reports the effects of changing membrane formation parameters, including polymer concentration, evaporation time and post casting annealing, on transport through integrally skinned asymmetric polyimide organic solvent nanofiltration membranes. The molecular weight cut off curve was most significantly affected by changes in the polymer concentration of the casting solution. Flux was observed to be sensitive to variations in several formation parameters. Scanning electron micrographs show three different morphologies present in the membranes, with a nanoporous nodular structure present at the top surface. The experimental transport data was interpreted using the intrinsic membrane parameters of permeability and pore size in the solution diffusion and pore flow models, respectively.
© 2007 Elsevier B.V. All rights reserved.

*Keywords:* Polyimide; Organic solvent nanofiltration; MWCO; Pore flow; Solution diffusion

## 1. Introduction

Organic solvent nanofiltration (OSN) has been advanced in recent years for many new applications [1] including solvent exchange, catalyst recovery and recycling [2,3], purifications and concentration. Reported polymeric OSN membranes are generally composites made from polydimethylsiloxane (PDMS) on polyacrylonitrile (PAN) [4–6] or integrally skinned asymmetric membranes made from polyimides (PI) [7,8]. PIs offer several attractive mechanical and physicochemical properties, including high glass transition temperatures ($T_g$), good thermal stability and good chemical stability in many solvents and weak acids [8–11]. In particular Lenzing P84 (Fig. 1), a BTDA-TDI/MDI co-polyimide of 3,3′,4,4′-benzophenone tetracarboxylic dianhydride and 80/20% toluenediamine and methylphenylenediamine, shows better chemical resistance than other PIs such as Matrimid and Sixef [9], making it a prime candidate for use in OSN. Commercially available polyimide membranes (Starmem™ [2] [12]) have been produced and are commercially available [13]. Novel materials and methods [14,15] for OSN membranes have emerged, but thus far research on OSN membranes has been mainly focused either towards the formation and morphological aspects of the membranes [16,17] or on the modelling of transport phenomenon [18–21] of established membranes.

The molecular weight cut off (MWCO) is determined by plotting rejection of solutes against solute MW and interpolating to determine the MW corresponding to a 90% rejection. Some control of the MWCO for PI membranes (pyromellitic dianhydride and 4,4′-diaminobenzophenone: PMDA–DABP) was previously demonstrated by Ohya et al. [22] and Okazaki et al. [23] through the variation of formation parameters (evaporation time, additives, etc.). The effect of several parameters (non-solvent additives in the dope solution and heat treatment) on the physical structure of the membranes made from Lenzing P84 was investigated by Qiao et al. [24] for use in pervaporation. It was observed that the addition of non-solvents to the dope solution resulted in different morphologies of the nodular structure but with little change to the separation factors. Annealing also resulted in the greatest change to flux and separation factors through densification of the separation layer. Thus far, there are no studies of integrally skinned OSN membranes that attempt to relate the membrane formation parameters to the membrane structure, and transport through the membrane. In

* Corresponding author. Tel.: +44 20 75945582; fax: +44 20 75945604.
*E-mail address:* a.livingston@imperial.ac.uk (A.G. Livingston).
[1] Current address: Departamento de Química, Faculdade de Ciências e Tecnologia, Universidade Nova de Lisboa, 2829-516 Caparica, Portugal.
[2] Starmem™ is a trademark of W.R. Grace and Co.

0376-7388/$ – see front matter © 2007 Elsevier B.V. All rights reserved.
doi:10.1016/j.memsci.2007.04.047

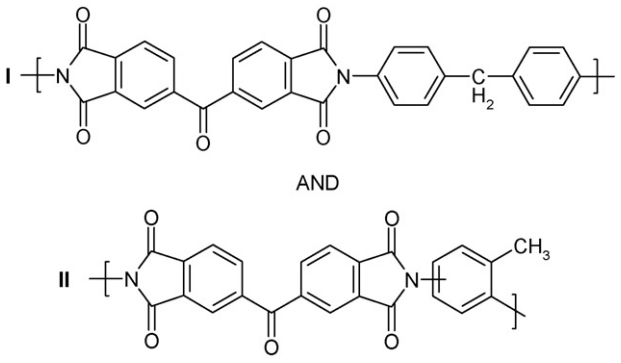


Fig. 1. Chemical structure of Lenzing P84 co-polyimide (20% **I** and 80% **II**).

this study we seek to address this challenge. Understanding this relationship would enable the tailoring of membranes to specific applications. Several casting parameters (e.g. evaporation time, polymer concentration, casting height and thermal annealing) have been varied in the manufacture of OSN membranes from the PI Lenzing P84. The solvent flux and MWCO curves of these membranes were determined under cross-flow at 30 bar and 30 °C over extended periods (24 h). A detailed study of membrane morphology was also performed using scanning electron microscopy (SEM). The key parameters of the solution diffusion (SD) and pore flow (PF) models were experimentally determined and used to correlate the data obtained for the MWCO curves and fluxes in an attempt to interpret the observed results. Experimental and calculated results were compared for membranes prepared under different conditions.

### 1.1. Theory/models

Different models have been developed for the description of membrane transport behaviour. In this work, simplified versions of two commonly used approaches, the SD and PF models have been utilized to gain some insight into the influence of membrane physical parameters on membrane transport. The two models presented in this paper differ in purposes from other works in that they are not used to make a direct comparison of their fit to the experimental data or their predictive ability. The intent of using the models is to interpret the transport data and evaluate the applicability of each model to the description of OSN transport via parameter fitting. Through this, we seek to establish a quantitative framework relating the membrane formation parameters to the intrinsic transport parameters such as membrane permeability and pore dimensions for the SD and PF models, respectively.

### 1.2. Solution diffusion

The solution diffusion model, first introduced by Lonsdale et al. [25], has been adopted by White [10] and Peeva et al. [26] to describe membrane transport in systems using PI OSN membranes. The important implications of this model with respect to the physical structure of the membrane are the lack of a porous layer, the diffusion of species without interaction, and the assumption of no pressure drop across the separating layer. Eq. (1) [27] describes the flux of a species $i$ across the membrane as being dependent on concentration and pressure.

$$J_i = P_i \left( x_{i,\mathrm{F}} - x_{i,\mathrm{P}} \exp\left[ -\frac{\upsilon_i(\Delta P)}{RT} \right] \right)$$

$$\text{with } P_i = \frac{D_i K_i}{l} \tag{1}$$

At osmotic equilibrium, where $\Delta P = \Delta \Pi$ and $J_i = 0$, Eq. (1) may be expressed as follows:

$$J_i = 0 = P_i \left( x_{i,\mathrm{F}} - x_{i,\mathrm{P}} \exp\left[ -\frac{\upsilon_i(\Delta \Pi)}{RT} \right] \right) \tag{2}$$

Eq. (2) can now be substituted into Eq. (1) yielding the following expression:

$$J_i = P_i x_{i,\mathrm{F}} \left( 1 - \exp\left[ -\frac{\upsilon_i(\Delta P - \Delta \Pi)}{RT} \right] \right) \tag{3}$$

In this two-parameter model, the solvent ($B$) and solute permeabilities ($P_i$) were calculated using simplifying assumptions and equations as shown by Peeva et al. [26]. The effects of concentration polarization are assumed to be negligible as a dilute feed solution was used. The solvent permeability may be experimentally determined from independent measurements of the pure solvent flux ($x_{i,\mathrm{F}} = 1$ and $\Delta \Pi = 0$) at different pressures using Eq. (4), which assumes that for small values of $z$, $1 - \exp(-z) = z$, since only the first term of Taylor series is significant.

$$J_{\text{solvent}} = B(\Delta P) \quad \text{where } B = \frac{P_i \upsilon_i}{RT} \tag{4}$$

Similarly, with the assumption that the concentration driving force is dominant at low pressures (4 bar) where $\exp(-z) \to 1$ when $z \to 0$, Eq. (1) can be simplified to Eq. (5). The solute permeabilities can thus be determined by measuring solute concentration and flux at low pressures ($\leq$4 bar).

$$J_i = P_i(x_{i,\mathrm{F}} - x_{i,\mathrm{P}}) \tag{5}$$

The solute and solvent permeabilities obtained from Eqs. (4) and (5) are then used to calculate the flux ($J_i^{\mathrm{SD}}$) and rejection ($R_i^{\mathrm{SD}}$) under the experimental conditions (30 bar and 30 °C) using Eq. (1) and the following equations:

$$\frac{x_{i,\mathrm{P}}}{\sum x_{i,\mathrm{P}}} = \frac{J_i}{\sum J_i} \tag{6}$$

$$J^{\mathrm{SD}} = \sum J_i \tag{7}$$

$$R_i^{\mathrm{SD}}(\%) = \left( 1 - \frac{x_{i,\mathrm{P}}}{x_{i,\mathrm{F}}} \right) \times 100 \tag{8}$$

These were then compared with experimental values obtained in independent experiments for membranes prepared under different conditions.

### 1.3. Pore flow

Most works on modelling of nanofiltration membranes assuming the presence of pores regard these membranes as

bundles of capillary tubes. In such cases, the Hagen–Poiseuille equation can be used to describe the relationship between the solvent flux and applied pressure [28]. The solvent permeability $L_p$ can be determined by a best fit plot of pure solvent flux against pressure.

$$J_v = \frac{r_p^2 \Delta P}{8\mu(\Delta x/A_k)} = L_p \Delta P \tag{9}$$

The hydrodynamic model used in this work is derived from the extended Nernst–Planck equation for the transport of solutes inside the membrane. This model has been successfully applied by several authors [29–32] for the description of nanofiltration transport. The equation consists of flux terms due to diffusive, electric field gradient and convection:

$$j_i = -K_{i,d} D_{i,\infty} \frac{dc_i}{dx} - \frac{z_i c_i D_{i,p}}{RT} F \frac{d\psi}{dx} + K_{i,c} c_i V \tag{10}$$

In this work, Eq. (10) is simplified to Eq. (11) by ignoring the transport term due to the electric field gradient:

$$j_i = -K_{i,d} D_{i,\infty} \frac{dc_i}{dx} + K_{i,c} c_i V \tag{11}$$

where $c_i$ is the solute concentration in the pore and $x$ is the axial position within the pore. The solute diffusive and convective hindrance factors $K_{i,d}$ and $K_{i,c}$ are functions of the ratio between the solute to pore radius ($\lambda_i = d_{i,s}/d_p$) [33]. Assuming a parabolic fully developed solute flow within the pore, the hindrance factors may be expressed as [30]:

$$K_{i,d} = 1.0 - 2.30\lambda_i + 1.154\lambda_i^2 + 0.224\lambda_i^3 \tag{12}$$

$$K_{i,c} = (2 - \Phi_i)(1.0 + 0.054\lambda_i - 0.988\lambda_i^2 + 0.441\lambda_i^3) \tag{13}$$

where $\Phi_i$ (partition coefficient) is the ratio of the average intra-pore concentration to that of the bulk solution at equilibrium. When the interactions between the solute and pore wall are purely steric, this may further be approximated as [30]:

$$\Phi_i = (1 - \lambda_i)^2 \tag{14}$$

Neglecting the effects of concentration polarization ($C_{i,m} = C_{i,f}$) and integrating Eq. (11) across the thickness of the membrane ($0 < x < \Delta x$) with the boundary conditions where $c_{i,x} = 0 = \Phi C_f$ and $c_{i,x=\Delta x} = \Phi C_p$ yields:

$$\frac{C_{i,p}}{C_{i,f}} = \frac{\Phi_i K_{i,c}}{1 - [1 - \Phi_i K_{i,c}] \exp(-P_{i,e})} \tag{15}$$

where the Peclet number is defined as follows:

$$P_{i,e} = \frac{K_{i,c} V \Delta x}{K_{i,d} D_{i,\infty} A_k} = \frac{K_{i,c}}{K_{i,d} D_{i,\infty}} \left( \frac{r_p^2 \Delta P}{8\mu J_v} \right),$$

$$D_{i,\infty} = \frac{kT}{6\pi\mu d_{i,s}} \tag{16}$$

The diffusivity in the bulk solution, $D_{i,\infty}$ can be calculated using the Stokes–Einstein equation [33]. The observed rejection of the solute can thus be presented as a function of $P_{i,e}$ and $\lambda_i$:

$$R_i^{PF} = 1 - \frac{C_{i,p}}{C_{i,f}} = 1 - \frac{\Phi_i K_{i,c}}{1 - [1 - \Phi_i K_{i,c}] \exp(-P_{i,e})} \tag{17}$$

Measurements of flux and rejection allow a value for $\lambda_i$ to be determined for each species using Eqs. (12)–(14) and (17). The effective molecular diameter ($d_{i,s}$) of each solute was determined in separate calculations by first optimising the solute structure solvated in the solvent of interest using Gaussian 03 molecular modelling software and ground state DFT, B3LY method with 6-31G+(d,p) basis set [32]. The Integral Equation Formalism Model Polarizable Continuum Model (IEFPCM) was used as the solvation method to calculate and optimise the solute structure in toluene the solvent of interest in this study. The smallest possible cylinder around the molecule was determined and the values of $H_i$ (the diameter) and $L_i$ (the length) were calculated. $d_{i,s}$ was further calculated using the following formula [34]:

$$d_{i,s} = \frac{\pi}{4} H_i + \frac{L_i}{2} \tag{18}$$

where $H_i$ is the diameter and $L_i$ the length of the smallest possible cylinder around the molecule of solute $i$.

The average $d_p$ ($d_P^{Avg}$) determined by Eq. (19) allowed the further estimation of $A_k/\Delta x$ using Eq. (9).

$$d_P^{Avg} = \frac{\sum d_{P,i}}{n} \tag{19}$$

where $n$ is the number of solutes.

## 2. Experimental

### 2.1. Chemicals

Lenzing P84 co-polyimide (Fig. 1) was purchased from HP polymer GmbH and used without any further purification or treatment. The solvents used for the preparation of membranes were *N*,*N*-dimethylformamide (DMF), 1,4-dioxane, isopropanol and toluene. Analytical grade toluene was used as the solvent. A series of solutes (decane, dodecane, tetradecane, hexadecane, docosane, hexacosane and tetraoctylammonium bromide) with increasing molecular weights (MW) were dissolved in toluene at low concentrations (0.2 wt%) to determine the MWCO curves for the membranes. Individual test solutes were used to obtain discrete peaks during analysis. All test solutes and chemicals were obtained from Sigma–Aldrich, UK.

### 2.2. Preparation of integrally skinned asymmetric OSN membranes

Lenzing P84 was dissolved in DMF and 1,4-dioxane (approximately 1:3) and stirred continuously at 50 °C overnight to obtain a homogeneous dope solution. The polymer solution was allowed to stand for a further 24 h to remove air bubbles at room temperature. The dope solution was used to cast films 200 μm thick on a polyester backing material (Hollytex 3329, Ahlstrom) using an adjustable casting knife on an automatic film applicator (Braive Instruments). Solvent was allowed to evaporate from the

Table 1
The composition of dope solution, the evaporation time and annealing temperature used in varying membrane properties

| Membrane | Dope solution composition (wt%) | | | Annealing temperature (°C) | Evaporation time (s) |
|---|---|---|---|---|---|
| | PI | DMF | Dioxane | | |
| M1 | 20 | 21 | 59 | – | 10 |
| M2 | 22 | 21 | 57 | – | 10 |
| M3 | 24 | 20 | 56 | – | 10 |
| M4 | 26 | 20 | 54 | – | 10 |
| M5 | 22 | 21 | 57 | – | 10 |
| M6 | 22 | 21 | 57 | – | 30 |
| M7 | 22 | 21 | 57 | – | 50 |
| M8 | 22 | 21 | 57 | – | 70 |
| M9 | 22 | 21 | 57 | 100 | 10 |
| M10 | 22 | 21 | 57 | 150 | 10 |
| M11 | 22 | 21 | 57 | 200 | 10 |
| M12 (dense film) | 22 | 21 | 57 | – | 24 h |
| M13 (100 μm) | 22 | 21 | 57 | – | 10 |
| M14 (200 μm) | 22 | 21 | 57 | – | 10 |
| M15 (300 μm) | 22 | 21 | 57 | – | 10 |

surface of the film at controlled time intervals after which the film was immersed, parallel to the surface, into a precipitation water bath at room temperature. The membranes were subsequently immersed in solvent exchange baths of isopropanol, and then toluene, to remove residual DMF and water. The membranes were then transferred from the toluene bath to a mineral oil bath. After the membranes were soaked in this bath, it was possible to handle the membranes in a "dry" state. Cracks were formed in the membranes if they were left to dry without the addition mineral oil as a conditioning agent. Table 1 summarises the conditions under which the membranes presented in this study were prepared. Evaporation occurred at ambient conditions (approximately 20 °C) expect for M13–M15 where warm conditions resulted in temperatures of 28–30 °C.

### 2.3. Preparation of homogeneous film (M12)

Lenzing P84 was dissolved according to the procedure mentioned above to produce the dope solution. A film was then cast on a flat glass plate with no backing material and allowed to evaporate to dryness for 24 h at room temperature under a constant flow of air.

### 2.4. Preparation of thermally annealed membranes

Membranes were prepared according to the procedure outlined in Section 2.2. Sample discs were cut out and sandwiched between glass plates before being placed in an oven at the specified temperature for 0.5 h. On removal, the membrane discs were allowed to cool naturally before testing in cross-flow. Some shrinkage of membranes M10 and M11 was observed with a visibly shinier surface.

### 2.5. Experimental apparatus and measurements

A laboratory bench scale cross-flow nanofiltration apparatus, shown schematically in Fig. 2, was used in all experiments. Membrane discs, of active area 14 $cm^2$, were cut out from the flat sheets and placed into 4 cross-flow cells connected in series. The feed solution was charged into a 5 L feed tank and re-circulated at a flow rate of 1.5 L $min^{-1}$ using a diaphragm pump (Hydra-Cell, Wanner International). Pressure was generated using a back pressure regulator located downstream of a pressure gauge. The cumulative pressure drop across the 4 cells was measured to be less than 0.5 bar. The re-circulating fluid was kept at 30 °C by a heat exchanger. During start-up, the mineral oil conditioning agent was removed by re-circulating pure solvent for an hour without applying any pressure and discarding the initial permeate. During operation, permeate samples were collected from individual sampling ports and feed samples were taken from the feed tank.

Pre-conditioning [20] of OSN membranes was necessary to achieve steady state fluxes and rejections. Fig. 3 shows the flux profile of membranes M1–M4 over time. For some membranes, steady state was only observed after up to 12 h of continuous operation, and so all experiments were conducted over a minimum of 24 h before samples were taken for rejection measurements. The flux was obtained by the equation:

$$J^{\mathrm{Obs}} = \frac{V}{At} \tag{20}$$

The experimental rejection of solute $i$ was calculated by the following equation:

$$R_i^{\mathrm{Obs}}(\%) = \left(1 - \frac{C_{\mathrm{p},i}}{C_{\mathrm{f},i}}\right) \times 100 \tag{21}$$

A plot of the rejection of the various solutes against the molecular weight allowed the MWCO of the membranes to be determined.

### 2.6. Analytical methods

Concentrations of solutes were determined using an Agilent 6850 Series II Gas Chromatograph with a flame ionization detector and an HP-1 column as the stationary phase. The temperature program selected was as previously published by Cherepitsa et

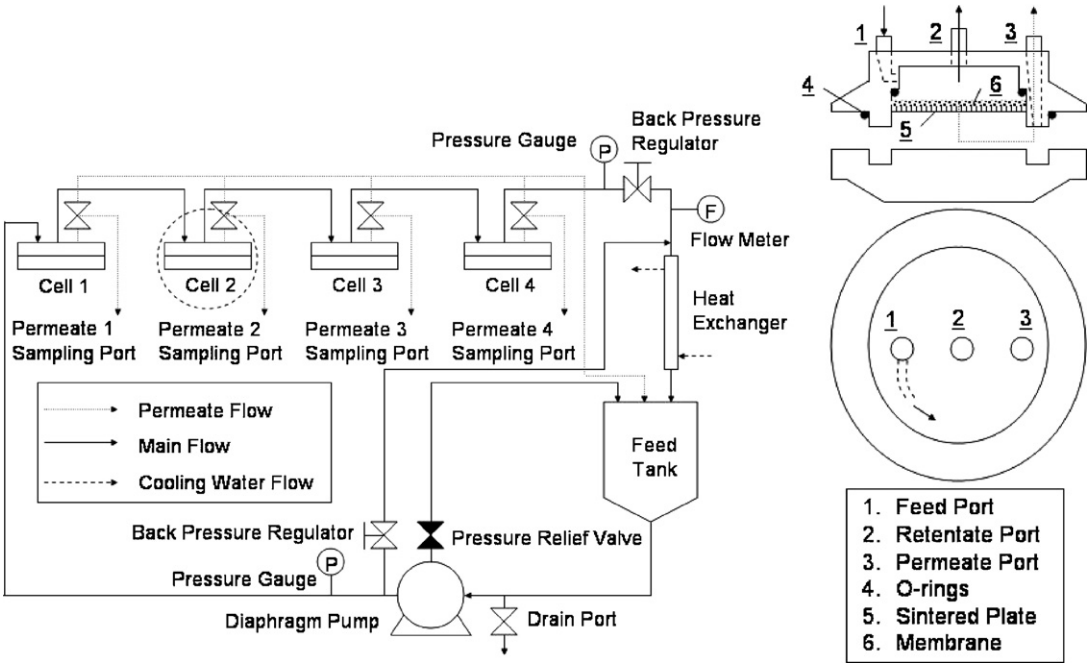


Fig. 2. Schematic of nanofiltration cross-flow apparatus; schematic of cross-section and top view of cross-flow cell.

al. [35] for petroleum fractions. The coefficient of variation was 3% for three independent observations. This analytical method allowed all solutes to be measured simultaneously to obtain the MWCO curves.

### 2.7. Scanning electron microscopy

Scanning electron micrographs were taken using a Leo 1525 field emission scanning electron microscope (FESEM). The membrane samples were first immersed in *n*-hexane to remove the conditioning oil and subsequently snapped in liquid nitrogen. The samples were then mounted onto the SEM stubs and sputtered using an Emitech K550 gold sputter coater. SEM conditions used were: 3 mm working distance, Inlens detector with an excitation voltage of 5 kV.

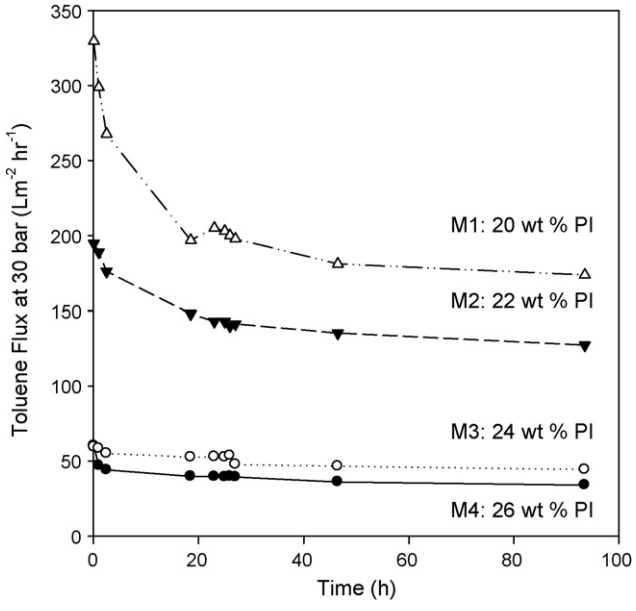


Fig. 3. Toluene flux profile of membranes M1–M4 over time.

## 3. Results and discussion

### 3.1. Effect of evaporation time and polymer concentration on membrane performance

Fig. 4 shows the effect of changing the evaporation time and dope concentration of PI on toluene flux at 30 bar. The flux was observed to decrease with increasing dope concentration from 170 L m$^{-2}$ h$^{-1}$ at 20 wt% PI to 30 L m$^{-2}$ h$^{-1}$ at 26 wt% PI. This may be explained by an increase in polymer concentration at the solvent/non-solvent interface during immersion precipitation. The volume fraction of the polymer in the final membrane also increases with higher polymer concentration, and consequently a resulting lower porosity might also contribute to the decrease in flux. This trend is consistent with that demonstrated by several authors [36,37] for different polymer substrates.

Increase in evaporation time showed a decrease in solvent flux from 110 L m$^{-2}$ h$^{-1}$ at 10 s to 50 L m$^{-2}$ h$^{-1}$ at 70 s for a membrane cast from 22 wt% PI dope solution. This behaviour was previously reported for systems in which volatile solvents such as acetone were used as the casting solvent [38], and was attributed to the increased thickness of the skin layer. In our system, in spite of the higher boiling point of the solvents used (DMF and 1,4-dioxane, b.p. of 153 and 102 °C, respectively), the results suggest that solvent evaporation is in part responsible for the observed change in fluxes. The sensitivity of flux to the evaporation time also makes reproducibility in the manufacture of OSN membranes between batches challenging.

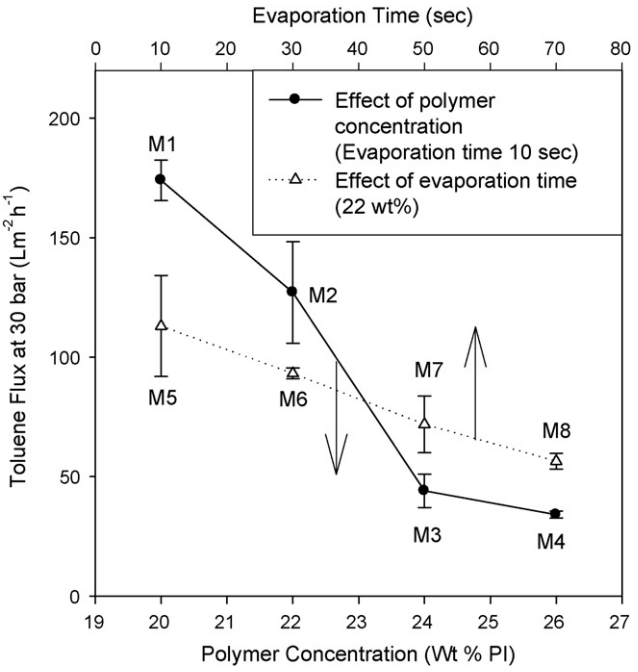


Fig. 4. Effect of evaporation time and polymer concentration in dope solution on toluene flux at 30 bar and 30 °C.

The MWCO curves for membranes at different polymer concentrations (M1–M4) are presented in Fig. 5A. A decrease in polymer concentration was observed to give a higher MWCO. This decrease was non-linear, with membranes at 24 and 26 wt% having a MWCO of 250 g mol$^{-1}$ and the membranes at 20 and 22 wt% at 310 g mol$^{-1}$. This reduction in rejection with an increase in flux (permeance) was also observed by Bulut et al. [39] for PI membranes. Interestingly, the MWCO for the membranes cast at different evaporation times and at the same polymer concentration (membranes M5–M8) all showed the same MWCO of 260 g mol$^{-1}$ (Fig. 5B). This suggests that both the solute and solvent flux are reduced at the same rate, so that while flux decreases, rejection remains constant.

SEM pictures of the membranes M1–M8 are shown in Figs. 6 and 7. Spherical features of 5–15 nm on the sample surface are attributed to the gold nanoparticles used to coat the membranes during the sputtering process. Figs. 6A and 7A show the cross-section of the membranes, as we tried to identify any significant morphological changes. Figs. 6B and 7B show a magnified cross-section of the top separation surfaces of the membranes. A membrane separation layer thickness of 200 nm for polyimide OSN membranes had been previously estimated [11,20] in the literature. The morphology observed within the top 100 nm of membrane consists of a matrix of tightly packed polymer nodules leaving small channels (<5 nm) between them. Some of these channels can be seen to reach the surface. The formation of polymer nodules on the surface layer have been described by Wienk et al. [40,41] and was observed by Carruthers et al. [42] for PI (Matrimid) membranes. No apparent increase of separation layer thickness with increasing evaporation time [43] could be observed for membranes M5–M8.

This seemingly nanoporous separating layer has interesting implications for the transport processes occurring within the layer. In particular, the solution diffusion model [27,44] assumes that there is no pressure drop across the separating layer. Whether this assumption can be valid for a nanoporous structure requires further detailed analysis. Clearly, further work is required to better understand flows across nanoporous films of semi-crystalline materials. It is possible that the nodular structure observed is an artefact of the SEM techniques used. However, later in the paper we investigate the effect of annealing and major changes in the membrane morphology leads us to conclude that changes in the nanostructure can be observed via SEM.

Figs. 6C and 7C show magnified cross-sections of the membranes. The pictures show that the membranes all exhibit a similar morphology with no obvious change with varying evaporation times and polymer concentrations. The only exception

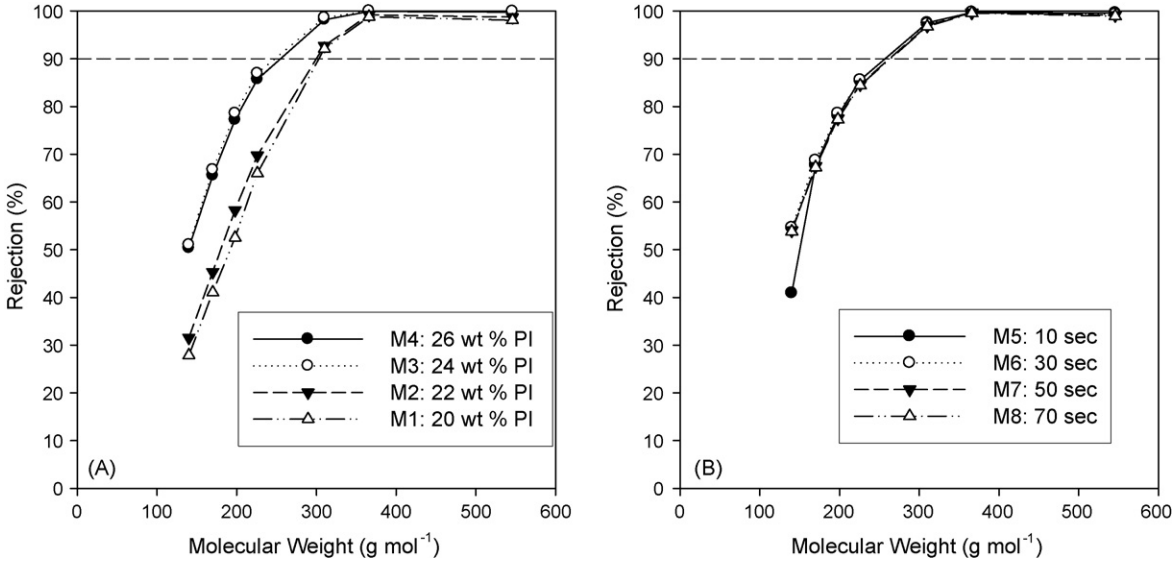


Fig. 5. Effect of polymer concentration (A) and evaporation time (B) on the MWCO in toluene at 30 bar and 30 °C. The coefficient of variation of the MWCO curves was calculated to be <2% for membranes produced under the same conditions.

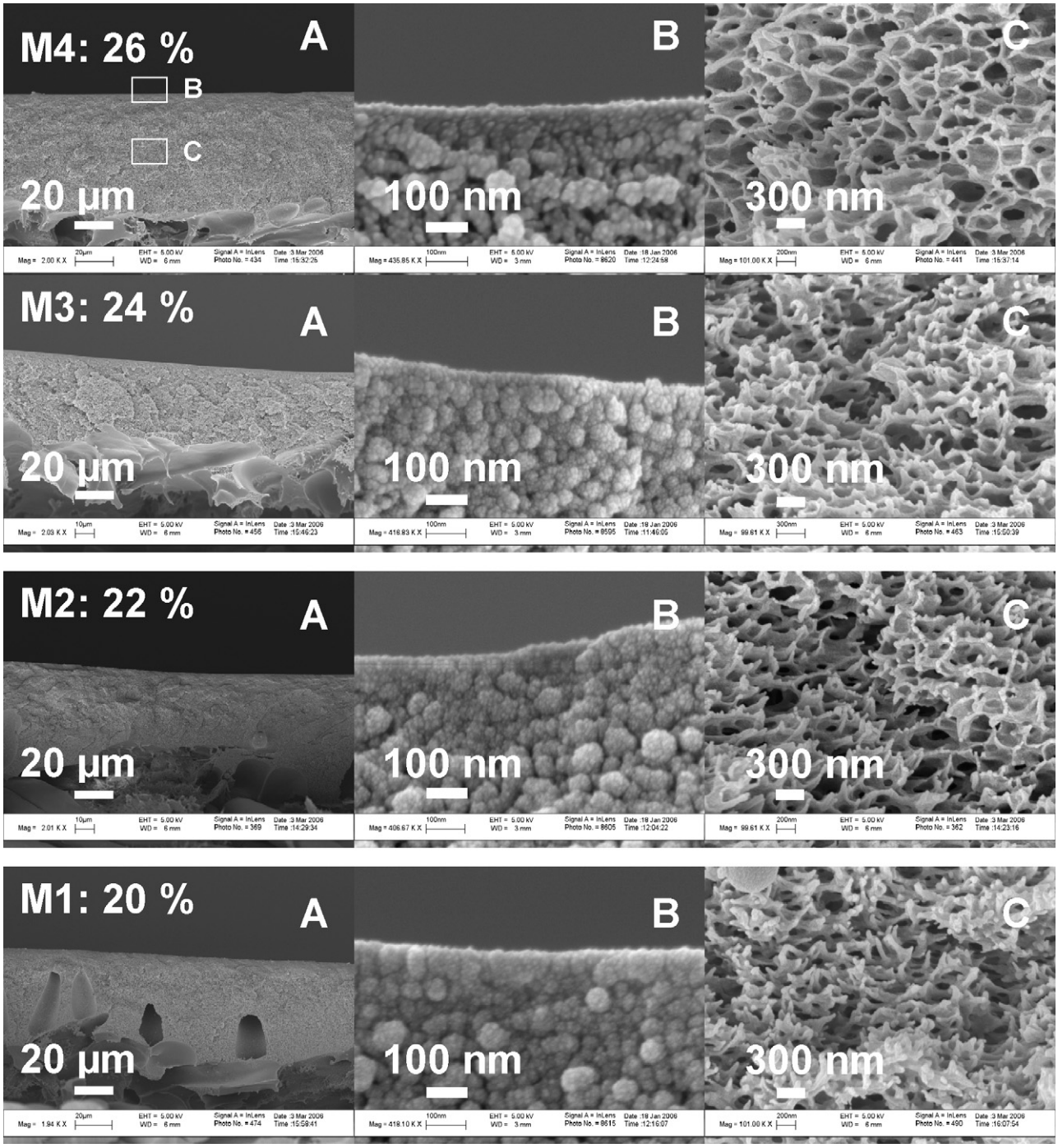


Fig. 6. Morphological changes with polymer concentration of PI membranes: (A) cross-section 2000×; (B) top layer 400,000×; (C) middle section 100,000×.

was the increasing presence of some macrovoids at lower polymer concentrations in membranes M1 and M2. This could be responsible for the higher fluxes observed and the greater compaction for the membranes at the lower polymer concentrations (Fig. 3). Further SEM pictures taken at various sections of the membrane also showed no apparent gradation of pore size within the spongy interconnected pores from the middle to the bottom of the membrane. An intermediate layer was also observed between the nodular structure at the top of the membranes and the interconnected pores.

Fig. 8 shows the morphology of membrane M2 before and after use. The membrane was observed to undergo little change in the top separation layer, whilst the supporting interconnected pores appeared to have a smaller pore size. Flux reduction observed during the initial conditioning phase of filtration might be explained by the decrease in pore size of the substructure observed in the membranes. This suggests that the transport through OSN membranes might be due to several mass transfer resistances, reflecting the asymmetric structure of the membrane, as suggested by Machado et al. [21].

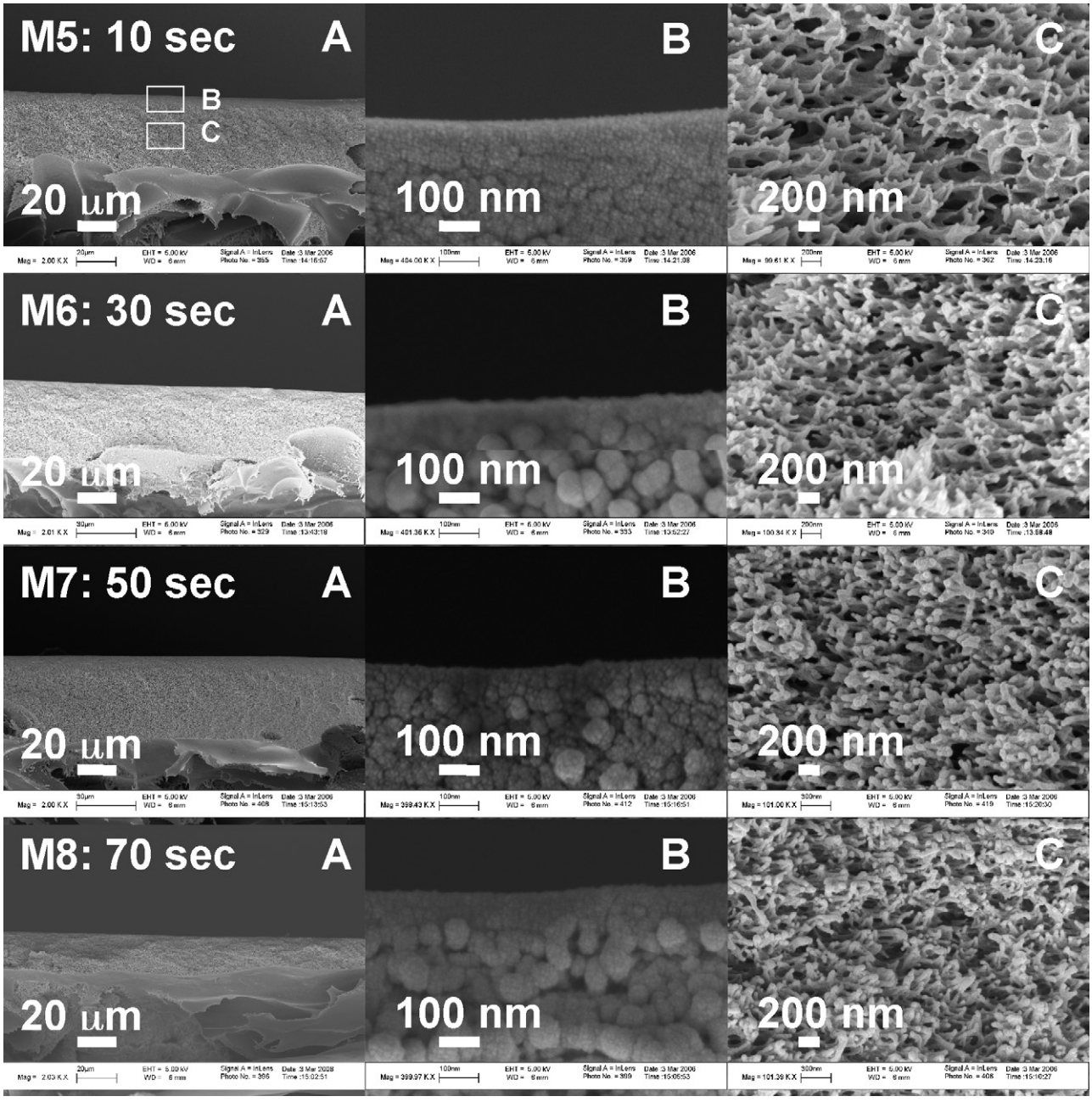


Fig. 7. Morphological changes with evaporation time of PI membranes: (A) cross-section 2000×; (B) top layer 400,000×; (C) middle section 100,000×.

To investigate further whether the thickness of the supporting layer has an effect on transport through the membrane, membranes (M13–M15) were cast at different heights. Fig. 9 shows the fluxes and MWCO curves for these membranes. The standard deviation for flux of the membranes was calculated to be ∼11%, indicating no obvious trend in the flux. The slight differences in flux were attributed to slightly different evaporation times between batches. The MWCO of the membranes also remained similar, indicating that the transport properties were independent of the casting thickness. SEM images also showed no difference in the overall morphology of the membranes. The only visible differences between the membranes were the final overall thickness of the membranes which were measured at 38, 66 and 80 μm for membranes cast at 100, 200 and 300 μm, respectively. We conclude that the supporting layer offers little resistance to mass transport.

The general observed morphology of the membranes is similar to that proposed by Reuvers and Smolders [45] and also observed by Qiao et al. [24] for Lenzing P84 membranes. The membranes consisted of three different zones/regions:

- a layer at the surface consisting of tightly packed polymer nodules with a depth of <500 nm;
- an intermediate layer of polymer nodules with less interconnected pores below the dense layer;

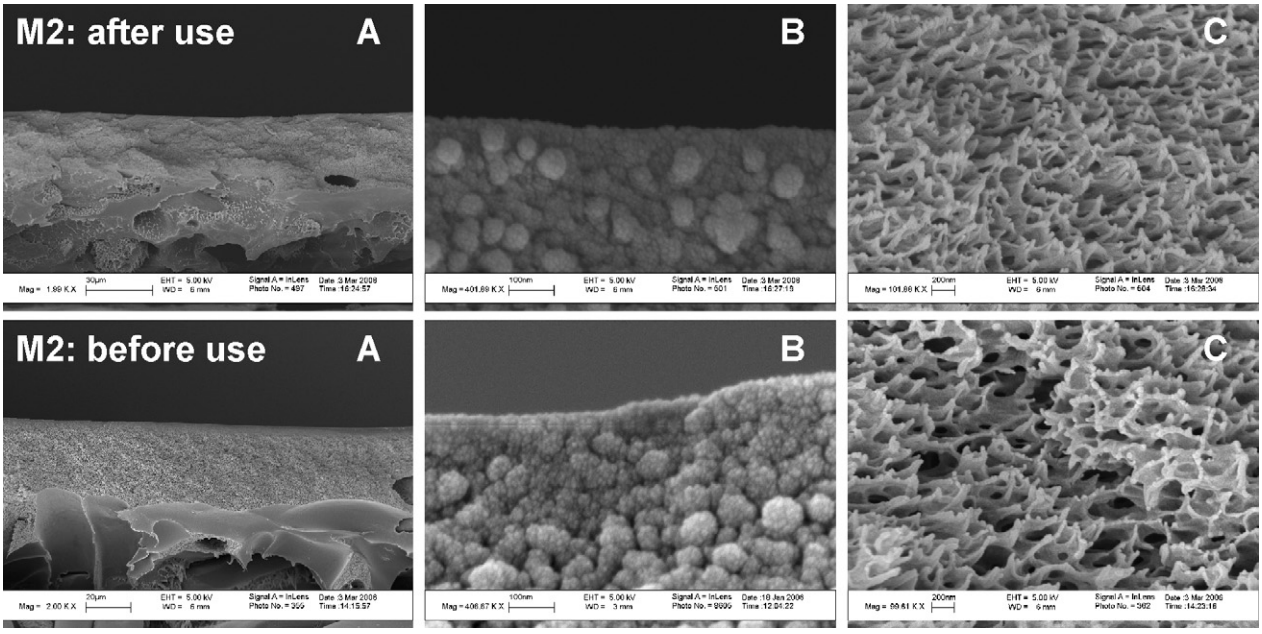


Fig. 8. Morphology change in membrane (M2) before and after use: (A) membrane cross-section (2000×); (B) top layer (400,000×); (C) interconnected pores (100,000×).

- an interconnected pore structure that extends through the membrane from the intermediate layer to the backing material with no apparent gradation of pore size.

Although three different morphologies were identified in the SEM study, it was difficult to discern the transition between these layers. One way to probe this transition between these layers is to try and reconstruct them as free-standing systems corresponding to the regions of the membrane. To this end, a homogeneous film was made by evaporating off all the solvent from a cast film (M16) resulting in the morphology shown in Fig. 10. This appeared dissimilar and denser than the top layer of any of the asymmetric membranes. No solvent flux (toluene at 30 bar) was observed across this membrane.

### 3.2. Thermal annealing

The thermal annealing of PI membranes has been studied by several authors for gas separation [46,47] and pervaporation [24,48,49]. This step has been shown to improve the performance in these processes by densification of the membrane films to remove defects and suppress plasticization. This usually results in increased selectivity at the expense of permeability [50]. In these cases, this observation has been attributed to the

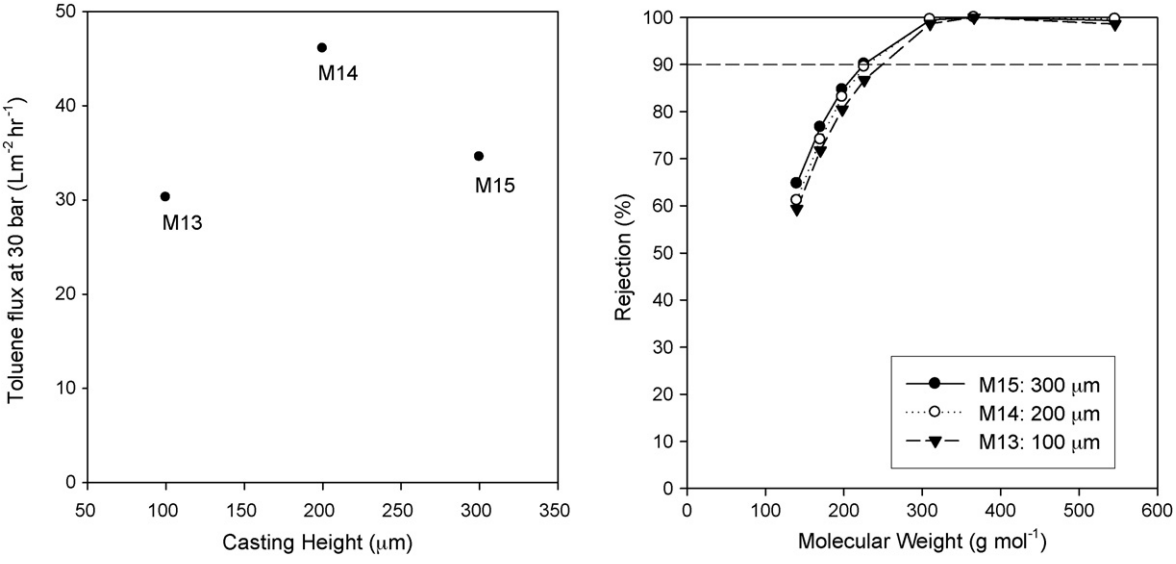


Fig. 9. Flux and rejection of 22 wt% membranes at different casting heights (M13–M15). Actual heights by SEM analysis—M13: 38 μm, M14: 66 μm and M15: 80 μm.

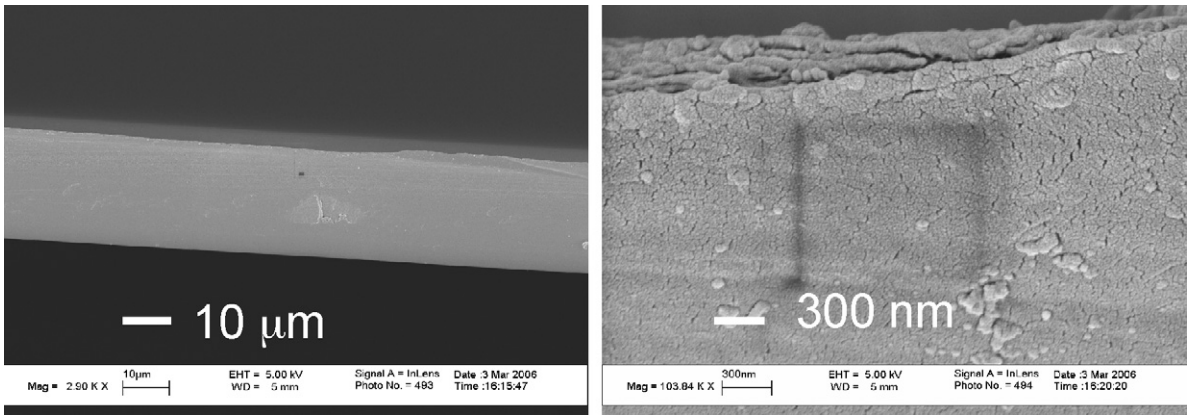


Fig. 10. Morphology of Lenzing P84 dense film (M16).

reorganization of the polymer chains at elevated temperatures to thermodynamically favoured structures and the simultaneous densification of the membrane. Fig. 11 shows the comparison of solvent flux and MWCO of membranes at different annealing temperatures. With the increase in annealing temperature, a decrease in flux was observed with a flux of 68 L m$^{-2}$ h$^{-1}$ for membrane M6 (with no thermal treatment) to no flux observed for membrane M11 (with thermal annealing at 200 °C). No physical changes were observed in the non-woven fabric over these temperatures. Interestingly, as with increasing evaporation times, the MWCO remains largely unaltered for membranes M9 and M10. SEM pictures (Fig. 12) of the membranes before and after annealing show a gradual loss of nanoporosity in the top separating layer of the membranes. The nodular structure observed in membranes without annealing was replaced with a continuous non-porous dense layer interspersed with nodules indicating that perhaps, some of the nodules have repacked to form a continuous layer. An obvious shrinkage of the annealed membranes was also observed. As alluded to previously, there is evident change in the nanostructure seen via SEM suggesting that the structures are not artefacts of the sample preparation technique. If the features were artefacts of the technique, the structures would remain constant across the different membranes.

These results show that within the parameter space explored in this work, while changing formation parameters (evaporation times and thermal annealing conditions) resulted in little change in the MWCO curves, the flux of each membrane varied significantly. The results suggest that the MWCO and flux might be independently varied. Also, the clear change from an appreciable to no flux for regular and annealed membranes suggests that the nanoporosity in the top layer is important in determining transport rates in these membranes.

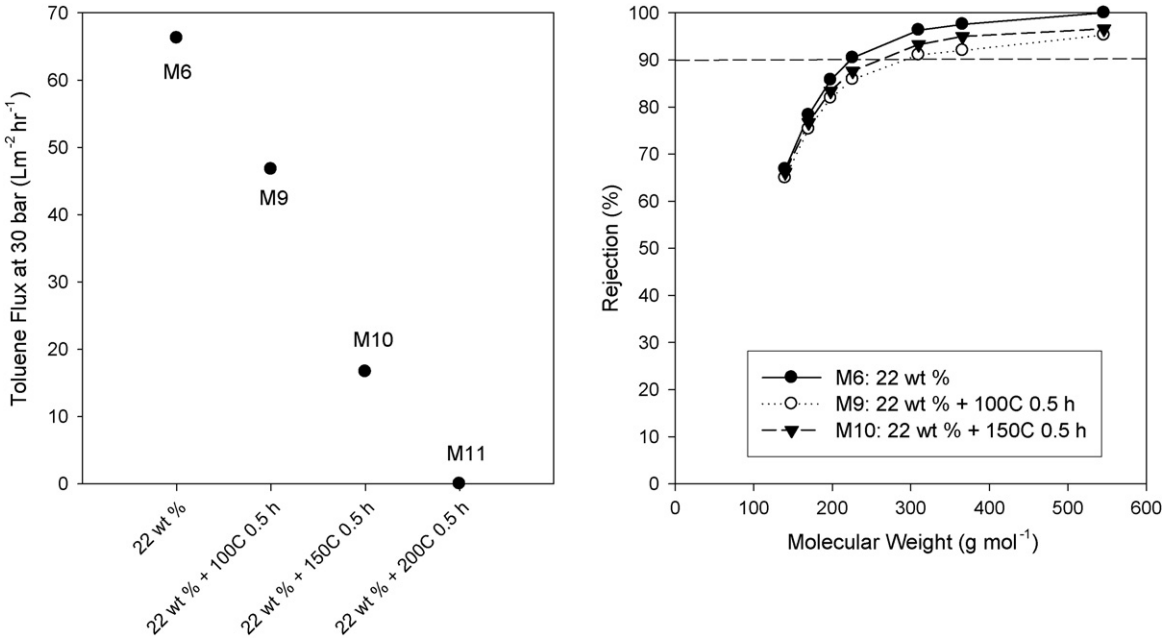


Fig. 11. Effect of thermal annealing on the flux and MWCO in toluene at 30 bar and 30 °C.

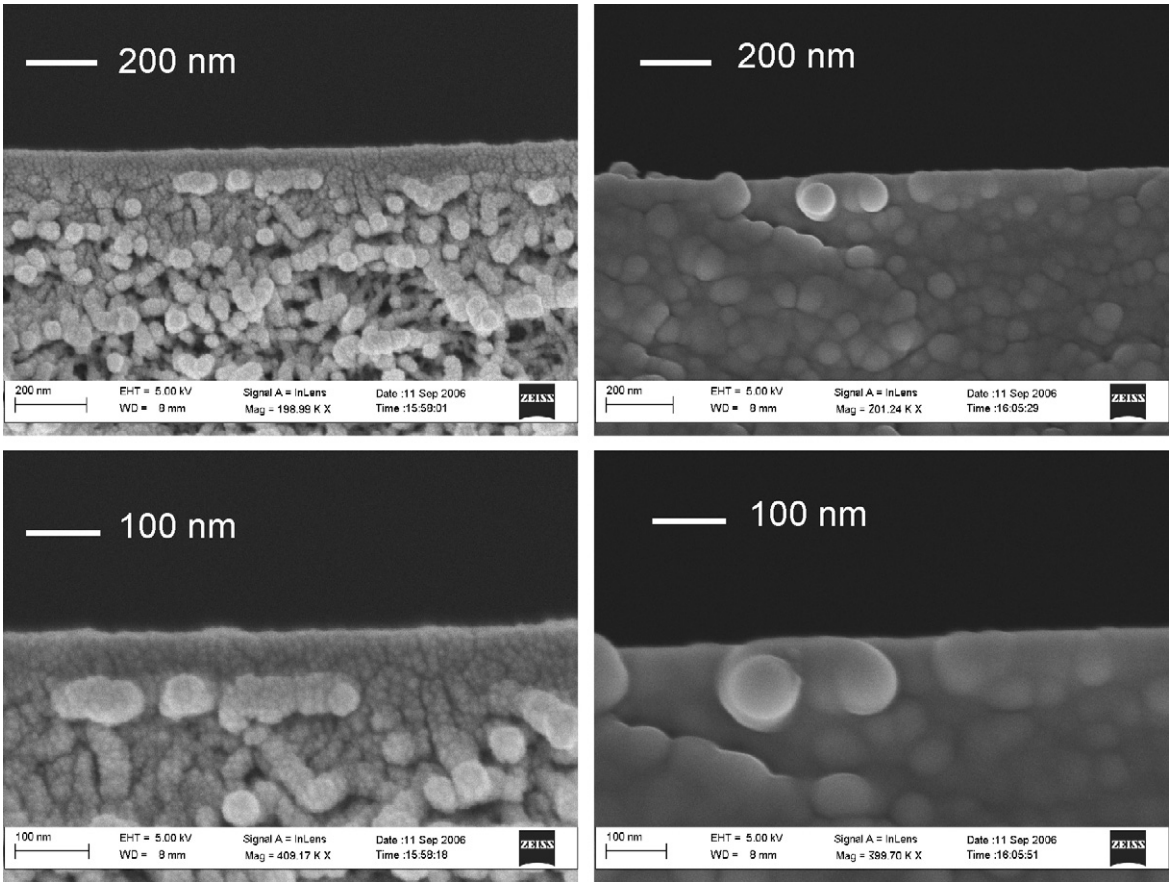


Fig. 12. Membrane morphology before (M2 left) and after annealing (M11) at 200 °C for 0.5 h.

### 3.3. Modelling

#### 3.3.1. Solution diffusion (SD)

Table 2 shows the experimentally determined permeabilities of the solvent and solutes for membranes M1–M4. The measured toluene permeabilities (M1–M4: 3.52–0.381 mol $m^{-2}$ $s^{-1}$) are similar to those obtained by White [10] (0.778 mol $m^{-2}$ $s^{-1}$) and Silva et al. [51] (0.585 mol $m^{-2}$ $s^{-1}$) for the polyimide membrane Starmem$^{TM}$ 122. M1 and M2 were observed to have higher permeabilities than Starmem$^{TM}$ 122 whilst M3 and M4 gave lower permeabilities. In all membranes, the solute permeabilities were observed to decrease with increasing molecular weight. However, TOABr (MW 546 g $mol^{-1}$) was observed to have a higher permeability than HCS (MW 366 g $mol^{-1}$) in all membranes in spite of a higher molecular weight. A similar observation was reported by White [10] with a lower permeability observed for branched molecules. This may be due to differences in shape and polarity between a quaternary ammonium salt (TOABr) and an alkane (HCS), resulting in unexpected permeabilities.

The solute permeabilities were determined by applying a low pressure (4 bar) across the membrane to determine the flux of the solutes calculating the permeabilities using Eq. (5). Fig. 13 shows the predicted and the actual values for the flux and MWCO curves for membranes M1–M8 using these values and applying the solution diffusion model at 30 bar. The model shows a reasonable fit for the prepared membranes.

Table 2
Experimentally determined solute and solvent permeabilities for use in the solution diffusion model

| Compound | Molecular weight (g $mol^{-1}$) | Molar volume ($cm^3$ $mol^{-1}$) | SD permeability ($\times 10^2$ mol $m^{-2}$ $s^{-1}$) | | | |
|---|---|---|---|---|---|---|
| | | | M1 | M2 | M3 | M4 |
| Toluene | 92 | 106 | 351.9 | 305.2 | 67.6 | 38.1 |
| *n*-Decane | 142 | 196 | 6.46 | 5.11 | 2.91 | 1.55 |
| Dodecane (DDC) | 170 | 225 | 3.58 | 2.68 | 1.06 | 0.569 |
| *n*-Tetradecane (TDC) | 198 | 260 | 2.06 | 1.52 | 0.659 | 0.353 |
| *n*-Hexadecane (HDC) | 226 | 292 | 1.19 | 0.865 | 0.408 | 0.227 |
| *n*-Docosane (DCS) | 310 | 399 | 0.255 | 0.184 | 0.114 | 0.0774 |
| Hexacosane (HCS) | 366 | 468 | 0.0340 | 0.0256 | 0.0211 | 0.0150 |
| Tetraoctylammonium bromide (TOABr) | 546 | 713 | 0.0413 | 0.0407 | 0.0427 | 0.0168 |

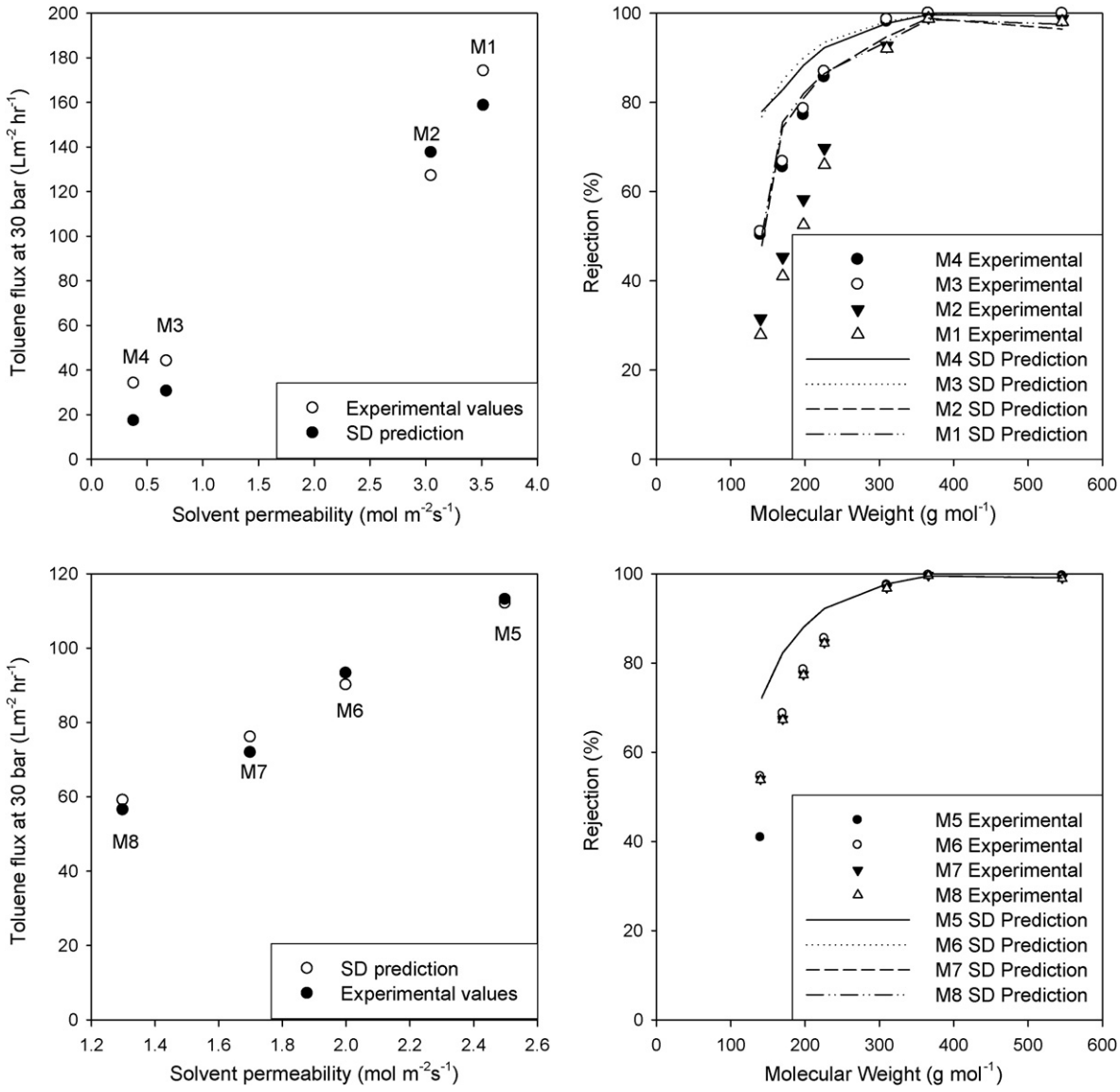


Fig. 13. Experimental values and solution diffusion predictions of flux and rejections for membranes M1–M8.

The increase in toluene permeability for membranes M1–M4 may be explained by an increased packing density of polymer chains leading to decreased flux with increasing polymer concentration. However, for membranes M5–M8, the apparent unchanged MWCO for the membranes represents a change in the solute permeability ($P_i$) in direct proportion to the change in the solvent permeability ($B$). For these membranes, it may be assumed that the membrane diffusion coefficient ($D_i$) and partition coefficient ($K_i$) are constant as manufacture aspects and membrane material were kept constant throughout. Hence a decrease in $P_i$ ($P_i = D_i K_i / l$) could imply an increase in the thickness of the separation layer $l$ with evaporation time. The increase in $l$ resulted in a proportional decrease in permeability of both solute and solvent resulting in the observed decrease in fluxes whilst maintaining the same rejections for the solutes. Assuming an initial separation thickness of 200 nm for M8 (evaporation time of 70 s), the change in flux between M5 (evaporation time 10 s) would represent a decrease in the membrane thickness of 50 nm. Although this morphological change could not be discerned in the SEM pictures, it can be seen from Figs. 6 and 7 that the predominant morphology within this length scale is of tightly packed polymer nodules. Fig. 14, obtained at a lower magnification, also shows that within a depth of 300 nm, the structure of the membrane changes considerably. Whilst it is difficult to define a discrete boundary for the active layer from the SEM micrographs, there is evidence that this active layer physically exists on the top of the asymmetric membrane, within a thickness no deeper than 300 nm. In addition, a change in the separation layer thickness assumed in the SD model could explain the apparent decrease in flux for the membranes with no change in the MWCO.

### 3.3.2. *Pore flow (PF)*

The presence of small channels between polymer nodules at the surface of the membranes suggests that the surface diffusion in pore flow mechanism might be of interest. Table 3 shows the

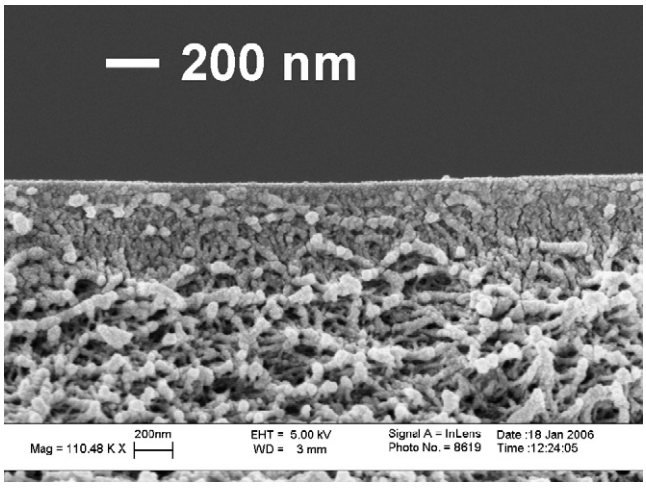


Fig. 14. Morphological changes in PI membranes.

molecular weight of the test solutes used in this study and their calculated effective molecular diameter ($d_S$). $d_S$ increased with the molecular weight of the solute except for TOABr. TOABr has a smaller value of $d_S$ in spite of a higher molecular weight than HCS. This implies that the rejection of the solutes can also be strongly linked to the shape of the molecule.

$L_p$ was determined from Eq. (9) by plotting flux against pressure for the different membranes. Table 4 shows a decrease in $L_p$ with increasing polymer concentration and evaporation time. Using the experimental values of $R_i$ and $J_v$ for each membrane, a value of $\lambda_i$ can be estimated for each solute. Assuming that the membrane comprises a bundle of uniform capillaries, an average $d_p$ can be estimated together with the corresponding values of $A_k/\Delta x$ (Table 4). The calculated pore diameter was observed to decrease with increasing polymer concentration in membranes M1 to M4, which represents an increase of 17% in $d_p$ with the increase of a polymer concentration of 20–26 wt%. This decrease in pore size was also observed by Ismail and Hassan [37] for a study in polysulfone nanofiltration membranes, where an increase of a polymer concentration from 19.6 to 32.8 wt% resulted in 54% $d_p$ decrease. The increased pore size at lower polymer concentrations can explain the higher flux and solvent permeabilities observed for these membranes.

For membranes M5–M8, $d_p$ was observed to remain the same for all membranes. The decrease in solvent permeability observed in the membranes can however be attributed to a decrease in $A_k/\Delta x$ from 3992 $m^{-1}$ for M5 to 2131 $m^{-1}$ for M8 as the evaporation time increases. Assuming $A_k$ remain constant for the membranes, this observation can be explained by a decrease in the thickness of separation layer in membrane M8–M5 by 100 nm.

The two models presented in this paper are able to adequately describe the observed phenomenon: Firstly, the observations of increased flux and decreased MWCO due to an increase in polymer concentration may be explained by either an increase in the separation layer thickness using the SD model or a decrease in pore size by the pore flow model. Secondly, the decrease in flux but unchanged MWCO due to an increase in the evaporation time maybe described by an increase in the separating layer thickness by both the SD and the SHP model. The proclivity for both models to be able to provide an explanation to the observed transport behaviour in OSN is testament to their continued widespread use to describe transport within the nanofiltration range.

Table 3
Effective molecular diameter of test solutes

| Compound | Molecular weight ($g\,mol^{-1}$) | Effective molecular diameter $d_S$ (nm) |
|---|---|---|
| Decane | 142 | 1.5 |
| DDC | 170 | 1.7 |
| TDC | 198 | 2.0 |
| HDC | 226 | 2.3 |
| DCS | 310 | 3.0 |
| HCS | 366 | 3.5 |
| TOABr | 546 | 3.1 |

Table 4
Estimated membrane permeability, pore size and $A_k/\Delta x$ values for membranes M1–M8

| Membrane | $L_p$ ($\times 10^{12}$ $L\,m^{-2}\,h^{-1}\,Pa^{-1}$) | $r_p$ (nm) | Standard deviation | $A_k/\Delta x$ ($m^{-1}$) |
|---|---|---|---|---|
| M1 | 16.93 | 3.53 | 0.8 | 1238 |
| M2 | 16.64 | 3.51 | 1.3 | 1814 |
| M3 | 4.76 | 3.10 | 1.7 | 8307 |
| M4 | 3.28 | 2.97 | 1.6 | 8873 |
| M5 | 10.46 | 3.51 | 3.0 | 3992 |
| M6 | 8.63 | 3.35 | 1.0 | 3624 |
| M7 | 6.65 | 3.37 | 1.0 | 2736 |
| M8 | 5.22 | 3.40 | 1.1 | 2131 |

## 4. Conclusion

In this paper, we have demonstrated the relationship between various formation parameters that affect the transport properties of PI OSN membranes. The following conclusions may be drawn from the presented results:

- Of the various parameters, the MWCO of the membranes seem to be most significantly affected by changes in the polymer concentration in the membranes. However significant increase of the MWCO would be at the expense of increased macrovoid formation and hence compaction in the membranes.
- The solvent flux was observed to vary with the various parameters except for the casting thickness of the membranes. Whilst it is difficult to ascertain which factor resulted in the most significant effect, it however does imply that the membrane flux is highly dependent upon many factors, and care must be taken to ensure reproducibility.
- Whilst SEM images could not be used to directly determine the presence of a separation layer in the membranes, the main structural features in the membranes could be examined by this means. The top separation layer of these membranes mainly consisted of polymer nodules with a degree of nanoporosity. The removal of this nanoporosity leads to flux decline and eventual termination of flux in the membranes.

- Both the shape and size of the solutes are important in the determination of the rejection.
- The performance of the membranes with changing polymer concentration and evaporation time can be adequately described by both the proposed SD and PF models. This does not allow selection of one model as being more 'accurate' than the other.

## Acknowledgements

The authors wish to acknowledge the support of *Pfizer Global Research and Development* for funding a studentship for YHST. FCF acknowledges financial support from Fundação para a Ciência e Tecnologia (SFRH/BPD/19369/2004).

## Nomenclature

| | |
|---|---|
| $A$ | membrane area ($m^2$) |
| $A_k$ | ratio of total cross-sectional pore area to effective membrane area |
| $B$ | SD solvent permeability ($mol\,m^{-2}\,s^{-1}\,Pa^{-1}$) |
| $c$, $C$ | PF solute concentration ($mol\,cm^{-3}$) |
| $D$ | SD membrane diffusion coefficient ($m^2\,s^{-1}$) |
| $D_p$ | hindered diffusion, $=K_d D_\infty$ ($m^2\,s^{-1}$) |
| $D_\infty$ | diffusivity in dilute bulk solution ($cm^2\,s^{-1}$) |
| $F$ | Faraday's constant ($C\,mol^{-1}$) |
| $H$ | cylinder diameter (m) |
| $j$ | PF solute flux per unit cross-sectional area and time ($mol\,cm^{-2}\,s^{-1}$) |
| $J^{Obs}$ | flux ($L\,m^{-2}\,h^{-1}$) |
| $J$ | SD flux ($mol\,m^{-2}\,s^{-1}$) |
| $J_v$ | PF solvent flux ($L\,m^{-2}\,h^{-1}$) |
| $K$ | SD membrane solvent partition coefficient |
| $l$ | SD active layer thickness (m) |
| $L$ | cylinder length/membrane thickness (m) |
| $L_p$ | PF solvent permeability ($L\,m^{-2}\,h^{-1}\,Pa^{-1}$) |
| $n$ | number if solutes |
| $P$ | permeability ($mol\,m^{-2}\,s^{-1}$) |
| $P_e$ | Peclet number |
| $\Delta P$ | pressure (Pa) |
| $r_p$ | PF pore radius (m) |
| $r_s$ | solute radius (m) |
| $R$ | gas constant ($Pa\,m^{-3}\,mol^{-1}\,K^{-1}$) |
| $R^{Obs}$ | rejection |
| $t$ | time (h) |
| $T$ | temperature (K) |
| $V$ | solute velocity ($m\,s^{-1}$) |
| $x$ | mole fraction |
| $\Delta x$ | PF active layer thickness (m) |
| $z$ | valence of ion |

*Greek letters*

| | |
|---|---|
| $\gamma$ | activity coefficient |
| $\lambda$ | ratio of solute to pore radius |
| $\mu$ | viscosity (Pa s) |
| $\Pi$ | osmotic pressure (Pa) |
| $\upsilon$ | molar volume ($cm^3\,mol^{-1}$) |
| $\Phi$ | partition coefficient |
| $\psi$ | electric potential (V) |

*Subscripts*

| | |
|---|---|
| f | feed |
| $i$ | component $i$ |
| p | permeate |

*Superscripts*

| | |
|---|---|
| Avg | average |
| Obs | observed |
| PF | pore flow |
| SD | solution diffusion |

## References

[1] U. Razdan, S.V. Joshi, V.J. Shah, Novel membrane processes for separation of organics, Curr. Sci. India 85 (2003) 761.
[2] H.T. Wong, C.J. Pink, F.C. Ferreira, A. Livingston, Recovery and reuse of ionic liquids and palladium catalyst for Suzuki reactions using organic solvent nanofiltration, Green Chem. 8 (2006) 373.
[3] H.T. Wong, Y.H. See-Toh, F.C. Ferreira, R. Crook, A.G. Livingston, Organic solvent nanofiltration in asymmetric hydrogenation: enhancement of enantioselectivity and catalyst stability by ionic liquids, Chem. Commun. (2006) 2063.
[4] C. Linder, M. Nemas, M. Perry, R. Katraro, Silicon derived solvent stable membranes, US 5,205,934 (1993).
[5] I.F.J. Vankelecom, K. De Smet, L.E.M. Gevers, A.G. Livingston, D. Nair, S. Aerts, S. Kuypers, P.A. Jacobs, Physio-chemical interpretation of the SRNF transport mechanism for solvents through dense silicone membranes, J. Membrane Sci. 231 (2004) 99.
[6] D.F. Stamatialis, N. Stafie, K. Buadu, M. Hempenius, M. Wessling, Observations on the permeation performance of solvent resistant nanofiltration membranes, J. Membrane Sci. 279 (2006) 424.
[7] L.S. White, I.F. Wang, B.S. Minhas, Polyimide membranes for separation of solvents from lube oil, US 5,264,166 (1993).
[8] L.S. White, Polyimide membranes for hyperfiltration recovery of aromatic solvents, US 6,180,008 (2001).
[9] M.A.M. Beerlage, Polyimide ultrafiltration membranes for non-aqueous systems, Ph.D. Thesis, University of Twente Enschede, 1994.
[10] L.S. White, Transport properties of a polyimide solvent resistant nanofiltration membrane, J. Membrane Sci. 205 (2002) 191.
[11] L.S. White, A.R. Nitsch, Solvent recovery from lube oil filtrates with a polyimide membrane, J. Membrane Sci. 179 (2000) 267.
[12] Starmem membranes, W.R. Grace & Co., http://www.membrane-extraction-technology.com/technologies/STARMEM%20Brochure.pdf, 2005.
[13] Membrane extraction technology (MET), http://www.membrane-extraction-technology.com/, 2006.
[14] V. Freger, A. Bottino, G. Capannelli, M. Perry, V. Gitis, S. Belfer, Characterization of novel acid-stable NF membranes before and after exposure to acid using ATR-FTIR, TEM and AFM, J. Membrane Sci. 256 (2005) 134.
[15] H.G. Hicke, I. Lehmann, G. Malsch, M. Ulbritcht, M. Beckor, Preparation and characterization of a solvent resistant and autoclavable polymer membrane, J. Membrane Sci. 198 (2002) 187.
[16] S.H. Yoo, J.H. Kim, J.Y. Jho, J. Won, Y.S. Kang, Influence of the addition of PVP on the morphology of asymmetric polyimide phase inversion membranes: effect of PVP molecular weight, J. Membrane Sci. 236 (2004) 203.

[17] J. Ren, Z. Li, F.S. Wong, Membrane structure control of BTDA-TDI/MDI (P84) co-polyimide asymmetric membranes by wet-phase inversion process, J. Membrane Sci. 241 (2004) 305.
[18] L. Braeken, R. Ramaekers, Y. Zhang, G. Maes, B.V.d. Bruggen, C. Vandecasteele, Influence of hydrophobicity on retention in nanofiltration of aqueous solutions containing organic compounds, J. Membrane Sci. 252 (2005) 195.
[19] D.R. Machado, D. Hasson, R. Semiat, Effect of solvent properties on permeate flow through nanofiltration membranes. Part I. Investigation of parameters affecting solvent flux, J. Membrane Sci. 163 (1999) 93.
[20] E. Gibbins, M.D. Antonio, D. Nair, L.S. White, L.M. Freitas dos Santos, I.F.J. Vankelecom, A.G. Livingston, Observations of solute flux and solute rejection across solvent resistant nanofiltration membranes, Desalination 147 (2002) 307.
[21] D.R. Machado, D. Hasson, R. Semiat, Effect of solvent properties on permeate flow through nanofiltration membranes. Part II. Transport model, J. Membrane Sci. 166 (2000) 63.
[22] H. Ohya, I. Okazaki, M. Aihara, S. Tanisho, Y. Negishi, Study on molecular weight cut-off performance of asymmetric aromatic polyimide membrane, J. Membrane Sci. 123 (1997) 143.
[23] I. Okazaki, H. Ohya, S.I. Semenova, M. Aihara, Y. Negishi, Study on molecular weight cut-off performance of asymmetric aromatic polyimide membrane "Effect of the additive agents", J. Membrane Sci. 141 (1998) 277.
[24] X. Qiao, T.S. Chung, K.P. Pramoda, Fabrication and characterization of BTDA-TDI/MDI (P84) co-polyimide membranes for the pervaporation dehydration of isopropanol, J. Membrane Sci. 264 (2005) 176.
[25] H.K. Lonsdale, U. Merten, R.L. Riley, Transport properties of cellulose acetate membranes to selected solutes, J. Appl. Polym. Sci. 9 (1965) 1341.
[26] L.G. Peeva, E. Gibbins, S.S. Luthra, L.S. White, R.P. Stateva, A.G. Livingston, Effect of concentration polarisation and osmotic pressure on flux in organic solvent nanofiltration, J. Appl. Polym. Sci. 236 (2004) 121.
[27] J.G. Wijmans, R.W. Baker, The solution-diffusion model: a review, J. Membrane Sci. 107 (1995) 1.
[28] S.I. Nakao, Models of membrane transport phenomena and their applications for ultrafiltration data, J. Chem. Eng. Jpn. 15 (1982) 200.
[29] W.R. Bowen, J.S. Welfoot, Modelling the performance of membrane nanofiltration—critical assessment and model development, Chem. Eng. Sci. 57 (2002) 1121.
[30] W.R. Bowen, A.W. Mohammad, N. Hilal, Characterisation of nanofiltration membranes for predictive purposes—use of salts, uncharged solutes and atomic force microscopy, J. Membrane Sci. 126 (1997) 91.
[31] J.L.C. Santos, P. de Beukelaar, I.F.J. Vankelecom, S. Velizarov, J.G. Crespo, Effect of solute geometry and orientation on the rejection of uncharged compounds by nanofiltration, Sep. Purif. Technol. 50 (2006) 122.
[32] P. Silva, A.G. Livingston, Effect of solute concentration and mass transfer limitations on transport in organic solvent nanofiltration-partially rejected solute, J. Membrane Sci. 280 (2006) 889.
[33] W.M. Deen, Hindered transport of large molecules in liquid-filled pores, AICHE J. 33 (1987) 1409.
[34] B. Van der Bruggen, J. Schaep, D. Wilms, C. Vandecasteele, A comparison of models to describe the maximal retention of organic molecules in nanofiltration, Sep. Sci. Technol. 35 (2000) 169.
[35] S.V. Cherepitsa, S.M. Bychkov, A.N. Kovalenko, A.L. Mazanik, N.M. Makoed, N.N. Gremyako, D.E. Kuzmenkov, Y.L. Luchinina, Determination of inspection parameters of diesel fuels, Chem. Tech. Fuels Oil 39 (2003) 364.
[36] M. Mulder, Basic Principles of Membrane Technology, Kluwer Academic Publishers, 1996.
[37] A.F. Ismail, A.R. Hassan, Formation and characterization of asymmetric nanofiltration membrane: effect of shear rate and polymer concentration, J. Membrane Sci. 270 (2006) 57.
[38] W.B. Krantz, R.J. Ray, R.L. Sani, K.J. Gleason, Theoretical study of the transport processes occurring during the evaporation step in asymmetric membrane casting, J. Membrane Sci. 29 (1986) 11.
[39] M. Bulut, L.E.M. Gevers, J.S. Paul, N.F.J. Vankelecom, P.A. Jacobs, Directed development of high-performance membranes via high-throughput and combinatorial strategies, J. Comb. Chem. 8 (2006) 168.
[40] I.M. Wienk, R.M. Boom, M.A.M. Beerlage, A.M.W. Bulte, C.A. Smolders, H. Strathmann, Recent advances in the formation of phase inversion membranes made from amorphous or semi-crystalline polymers, J. Membrane Sci. 113 (1996) 361.
[41] I.M. Wienk, T. Vandenboomgaard, C.A. Smolders, The formation of nodular structures in the top layer of ultrafiltration membranes, J. Appl. Polym. Sci. 53 (1994) 1011.
[42] S.B. Carruthers, G.L. Ramos, W.J. Koros, Morphology of integral-skin layers in hollow-fiber gas-separation membranes, J. Appl. Polym. Sci. 90 (2003) 399.
[43] H. Kawakami, M. Mikawa, S. Nagaoka, Formation of surface skin layer of asymmetric polyimide membranes and their gas transport properties, J. Membrane Sci. 137 (1997) 241.
[44] D.R. Paul, Reformulation of the solution-diffusion theory of reverse osmosis, J. Membrane Sci. 241 (2004) 371.
[45] A.J. Reuvers, C.A. Smolders, Formation of membranes by means of immersion precipitation. Part II. The mechanism of formation of membranes prepared from the system cellulose acetate-acetone-water, J. Membrane Sci. 34 (1987) 67.
[46] H. Kawakami, M. Mikawa, S. Nagaoka, Gas transport properties in thermally cured aromatic polyimide membranes, J. Membrane Sci. 118 (1996) 223.
[47] A. Bos, I.G.M. Punt, M. Wessling, H. Strathmann, Plasticization-resistant glassy polyimide membranes for $CO_2/CO_4$ separations, Sep. Purif. Technol. 14 (1998) 27.
[48] W.F. Guo, T.S. Chung, Study and characterization of the hysteresis behavior of polyimide membranes in the thermal cycle process of pervaporation separation, J. Membrane Sci. 253 (2005) 13.
[49] F. Zhou, W.J. Koros, Study of thermal annealing on Matrimid(R) fiber performance in pervaporation of acetic acid and water mixtures, Polymer 47 (2006) 280.
[50] R.W. Baker, Membrane Technology and Applications, John Wiley & Sons Ltd., 2004.
[51] P. Silva, S. Han, A.G. Livingston, Solvent transport in organic solvent nanofiltration membranes, J. Membrane Sci. 262 (2005) 49.